



This is a repository copy of *Geometrically nonlinear extended isogeometric analysis for cohesive fracture with applications to delamination in composites*.

White Rose Research Online URL for this paper:
<https://eprints.whiterose.ac.uk/181913/>

Version: Accepted Version

Article:

Fathi, F. orcid.org/0000-0003-0789-3203 and de Borst, R. orcid.org/0000-0002-3457-3574
(2021) Geometrically nonlinear extended isogeometric analysis for cohesive fracture with applications to delamination in composites. *Finite Elements in Analysis and Design*, 191. 103527. ISSN 0168-874X

<https://doi.org/10.1016/j.finel.2021.103527>

© 2021 Elsevier B.V. This is an author produced version of a paper subsequently published in *Finite Elements in Analysis and Design*. Uploaded in accordance with the publisher's self-archiving policy. Article available under the terms of the CC-BY-NC-ND licence (<https://creativecommons.org/licenses/by-nc-nd/4.0/>).

Reuse

This article is distributed under the terms of the Creative Commons Attribution-NonCommercial-NoDerivs (CC BY-NC-ND) licence. This licence only allows you to download this work and share it with others as long as you credit the authors, but you can't change the article in any way or use it commercially. More information and the full terms of the licence here: <https://creativecommons.org/licenses/>

Takedown

If you consider content in White Rose Research Online to be in breach of UK law, please notify us by emailing eprints@whiterose.ac.uk including the URL of the record and the reason for the withdrawal request.



eprints@whiterose.ac.uk
<https://eprints.whiterose.ac.uk/>

A geometrically nonlinear extended isogeometric analysis for cohesive fracture: Application in delamination of composites

Farshid Fathi, René de Borst*

Department of Civil and Structural Engineering, University of Sheffield, S1 3JD, UK

Abstract

The objective of this study is to provide a geometrically nonlinear extended isogeometric analysis for cohesive fracture, with an application to delamination in composite. Employing superior features of isogeometric analysis, namely higher-order inter-element continuity, renders the difference between this approach and the customary Lagrangian interpolation, making the former ideal for stress estimation across element boundaries. Also, the higher-order continuity provided by isogeometric analysis can effectively deal with higher-order differential equations, i.e. a scene is set for potential future studies whose analysis requires higher-order continuity. Bézier extraction is employed to cast the formulation in a finite element datastructure. Use of a sign function for the enhanced field lessens the assumptions taken for governing equations compared to a step function, and subsequently yields a new discretised formulation presented here. Next, the role of the geometric contribution of the linearised interface tangent and its implications on the convergence are studied. Several practical examples in industry are exploited to illustrate the viability of such approach compared to the conventional finite element counterpart.

Keywords: Extended isogeometric analysis, Cohesive fracture, geometric nonlinearity, Bézier extraction, Heaviside sign function

*Corresponding author

Email address: r.deborst@sheffield.ac.uk (René de Borst)

1. Introduction

In the contemporary industry, for instance dealing with slender plies of laminated composites which are prone to delamination, large deformations and rotations occur inevitably complicating the production of a sound material. A priori knowledge of the critical failure mode facilitate industrial procedure to lessen the try and error attempts, a costly approach to understand fracture mechanism. Accordingly, to numerically analyse a problem entailing such issues, a geometrically nonlinear continuum is equipped with fracture mechanics. It is noted that the application is not limited to industrial composites, but also has dragged into a variety of disciplines, e.g. fluid flow in progressively fracturing porous medium [1], or damage analyses in ductile fracture [2] and biological composites [3].

From a mathematical modelling point of view, presence of a discontinuity elevates the complexity of the analysis since a combination of nonlinear continuum and fracture mechanics is required. This has already been investigated in [4] with interface elements and in [5] as a partition of unity method [6] which allows for modelling and propagating an arbitrary discontinuity free of the underlying mesh lay-out [7, 8, 9], which is also known as eXtended Finite Element Method (XFEM). Though robust in results, [5] has employed a step function to extract the formulation, necessitating an additional assumption for the vector normal to the crack profile. This assumption has been relaxed here using a sign function to define normal vectors for sides and the profile of the crack separately. Next, similar to other customary finite element approaches, Lagrange interpolation has been utilised in [5] which provides C^0 -continuity across element boundaries. By way of contrast, B-splines guarantee higher-order inter-element continuity within IsoGeometric Analysis (IGA) which can be applied in higher-order differential equations, e.g. fluid flow in porous media. Moreover, IGA facilitates exact parametrisation of the geometry, a significant feature required in the industry for a precise outcome.

In order to successfully capture any stress concentration stemmed from a

discontinuity, such as a crack, an additional displacement field could be utilised to distinctly capture this gradient. In other words, the first displacement field would capture the regular deformation while gradient estimation underlying the discontinuity would be achieved by the second one [7, 8, 9]. This method was
35 coined as Extended finite element method since it was first built on the customary finite element platform. Recently, eXtended IsoGeometric Analysis (XIGA) was developed for cohesive fracture, an attempt to incorporate the interesting features of IGA into the extended method. The absence of a proper compatibility between the aforementioned two fields and, unlike Linear Elastic Fracture
40 Mechanics (LEFM) [10], complexities risen from enrichment of individual control points in cohesive fracture necessitated developing such method [11]. Now this method has been put into test within the geometric nonlinearity.

Herein, we propose XIGA for the geometric nonlinearity. Similar to [11] *shifting* technique will be utilised to enforce compatibility in the direction perpendicular to the crack path. The inter-element share of control points governing B-splines or Non-Uniform Rational B-Splines (NURBS) complicates this
45 technique, as a price paid for higher-order continuity at element boundaries. In other words, the lack of Kronecker-delta property in IGA extends the discontinuous domain to multiple element rows perpendicular to the crack path,
50 which is unlike to the single element row containing crack profile in Lagrange interpolation-based approaches [11], namely XFEM. Also, to remove the effect of discontinuity in front of the crack and to avoid ultra-fine meshes ahead of the crack tip needed for the cohesive fracture [11], a *blending* technique has been adopted. Finally, Bézier extraction has been exploited to cast XIGA in
55 an element-wise format compatible with finite element datastructure. Isotropic linear elasticity governs a rate independent hyperelastic bulk, while NURBS has been utilised as the basis functions.

This contribution starts with kinematics of displacement discontinuity, followed by equilibrium equations governing the bulk and the discontinuity. Next
60 are variational formulations to achieve the governing weak forms and discrete equations for XIGA using a Bézier extraction-based NURBS. Also, aspects of

compatibility and implementation are studied as a separate section. The paper concludes with case studies assessing the delamination and its propagation, ensued by geometric nonlinearity issues realised of instabilities and contribution
65 role of linearised interface tangent.

2. Nonlinear displacement field and constitutive equations

A body undergoing the geometrical nonlinearity is shown in Figure 1. The equation of motion $\Phi(\mathbf{X}, t)$ maps a point \mathbf{X} in the reference (material) configuration onto the corresponding point \mathbf{x} in the spatial (current) one ($t > 0$). In
70 order to establish a discontinuous geometrically non-linear approach, displacement discontinuity is cast within an extended approach. Next is the description of the governing equations at the bulk and the discontinuity to set the scene for a variational formulation.

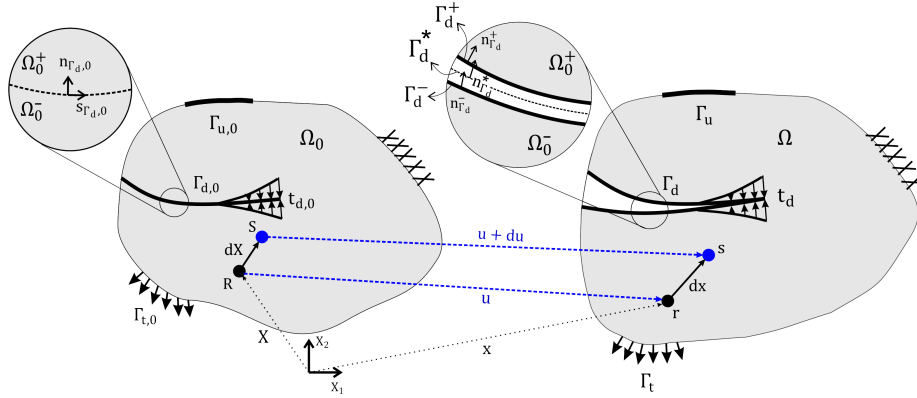


Figure 1: Boundary value problem with cohesive tractions. Reference configuration (left) is mapped onto the spatial one (right) through the motion $\Phi(\mathbf{X}, t)$. Also, mapping of a vector from the material to current configuration is illustrated in the figure, where \mathbf{u} and $\mathbf{u} + d\mathbf{u}$ are functions of the regular displacement $\hat{\mathbf{u}}$ and the displacement jump $\tilde{\mathbf{u}}$.

2.1. Kinematics of the displacement discontinuity

75 Based on the partition of unity, non-linear kinematic relations can be cast in an extended approach,

$$\Phi(\mathbf{X}, t) := \mathbf{x}(\mathbf{X}, t) = \mathbf{X} + \hat{\mathbf{u}}(\mathbf{X}, t) + \mathcal{H}_{\Gamma_{d,0}}(\mathbf{X})\tilde{\mathbf{u}}(\mathbf{X}, t) \quad (1)$$

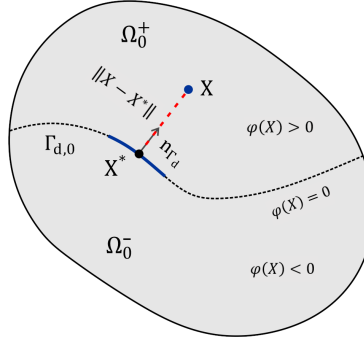


Figure 2: Signed distance function in the material description. The point \mathbf{X}^* is the closest projection of the point \mathbf{X} onto the discontinuity $\Gamma_{d,0}$

where $\hat{\mathbf{u}}(\mathbf{X}, t) = \mathbf{N}(\mathbf{X})\mathbf{a}(\mathbf{X}, t)$ and $\tilde{\mathbf{u}}(\mathbf{X}, t) = \mathbf{N}(\mathbf{X})\mathbf{b}(\mathbf{X}, t)$, while \mathbf{N} denotes the set of finite element shape functions. \mathbf{a} and \mathbf{b} indicate the regular and enhanced degrees of freedom, respectively. The Heaviside function in the reference con-
80 figuration $\mathcal{H}_{\Gamma_{d,0}}$ is defined on the signed distance function $\varphi(x)$ [11] (see Figure 2),

$$\mathcal{H}_{\Gamma_{d,0}}(\mathbf{X}) := \text{sign}(\varphi(\mathbf{X})) = \begin{cases} -1 & \text{if } \varphi(\mathbf{X}) < 0 \\ 0 & \text{if } \varphi(\mathbf{X}) = 0 \\ +1 & \text{if } \varphi(\mathbf{X}) > 0 \end{cases} \quad (2)$$

Note that the *step* function used in Wells *et al.* [5] is substituted for the *sign* function here, whose implications will be discussed in the remainder of the manuscript. Taking the gradient of the equation of motion in Equation (1) the
85 deformation gradient results [5],

$$\mathbf{F} := \nabla_{\mathbf{X}}\Phi = \hat{\mathbf{F}} + \mathcal{H}_{\Gamma_{d,0}}(\mathbf{X})\tilde{\mathbf{F}} + 2\delta_{\Gamma_{d,0}}(\tilde{\mathbf{u}} \otimes \mathbf{n}_{\Gamma_{d,0}}). \quad (3)$$

$\hat{\mathbf{F}} = \mathbf{1} + \nabla_{\mathbf{X}}\hat{\mathbf{u}}$ and $\tilde{\mathbf{F}} = \nabla_{\mathbf{X}}\tilde{\mathbf{u}}$, while $\mathbf{n}_{\Gamma_{d,0}}$ being the vector normal to the discontinuity in the reference configuration and $\mathbf{1}$ denoting the identity matrix.

As observed in Figure 1, vectors normal to crack path and sides will differ naturally from one another within geometrical nonlinearity. Note that, with a step function (0 and 1 values), vectors normal to the sides of the crack are defined
90 on the Nanson's relation [5], and the mean of the step function values (0.5) would be utilised for the crack path exclusively [5]. By way of contrast, exploiting a sign function as the Heaviside function precludes manipulative definition of the normal vector for the crack path,

$$\mathbf{n}_{\Gamma_d}^- = \det(\hat{\mathbf{F}} - \tilde{\mathbf{F}})((\hat{\mathbf{F}} - \tilde{\mathbf{F}})^T)^{-1} \mathbf{n}_{\Gamma_{d,0}} \frac{d\Gamma_{d,0}}{d\Gamma_d^-} \quad (4a)$$

$$\mathbf{n}_{\Gamma_d}^* = \det(\hat{\mathbf{F}})((\hat{\mathbf{F}})^T)^{-1} \mathbf{n}_{\Gamma_{d,0}} \frac{d\Gamma_{d,0}}{d\Gamma_d^*} \quad (4b)$$

$$\mathbf{n}_{\Gamma_d}^+ = \det(\hat{\mathbf{F}} + \tilde{\mathbf{F}})((\hat{\mathbf{F}} + \tilde{\mathbf{F}})^T)^{-1} \mathbf{n}_{\Gamma_{d,0}} \frac{d\Gamma_{d,0}}{d\Gamma_d^+} \quad (4c)$$

95 with * denoting the crack path, see Figure 1.

2.2. Governing equations at the bulk

In general, *elasticity* can be expressed as a constitutive equation dependent on the current state of deformation. From a continuum mechanics perspective, the stress measure of any arbitrary point in material description \mathbf{X} is only
100 a function of the deformation gradient, $\mathbb{P} = \mathbb{P}(\mathbf{F}(\mathbf{X}), \mathbf{X})$ [12]. Note that \mathbb{P} denotes the *first Piola-Kirchhoff* (nominal) stress which is the work conjugate of the deformation gradient \mathbf{F} . *Hyperelasticity* denotes the condition when the material behaviour is path-independent, i.e. it is only a function of the initial and current states. Accordingly, the stored *strain energy function* reads [12],

$$\Psi(\mathbf{F}(\mathbf{X}), \mathbf{X}) = \int_{t_0}^t \mathbb{P}(\mathbf{F}(\mathbf{X}), \mathbf{X}) : \dot{\mathbf{F}} dt, \quad \dot{\Psi} = \mathbb{P} : \dot{\mathbf{F}}. \quad (5)$$

105 A Neo-Hookean material $\Psi = \frac{\mu}{2} (I_1 - 3) - \mu \ln J + \frac{\lambda}{2} (\ln J)^2$ has been adopted in this manuscript, where μ and λ are Lamé's coefficients, $J = \det \mathbf{F}$, and

$I_1 = \text{trace}(\mathbf{C})$ denotes an invariant where $\mathbf{C} = \mathbf{F}^T \mathbf{F}$ is the right Cauchy tensor [12]. Derivatives of invariants and strain energy function can be found in [3, 12].

In the absence of the acceleration and body forces, the strong form of the
 110 equilibrium equation in the reference configuration reads:

$$\left\{ \begin{array}{ll} \nabla_{\mathbf{X}} \cdot \mathbb{P} = 0 & \mathbf{X} \in \Omega_0 \\ \mathbf{u} = \bar{\mathbf{u}}_0 & \mathbf{X} \in \Gamma_{u,0} \\ \mathbf{n}_0 \cdot \mathbb{P} = \bar{\mathbf{t}}_0 & \mathbf{X} \in \Gamma_{t,0} \\ \mathbf{n}_{\Gamma_{d,0}} \cdot \mathbb{P} = \mathbf{t}_{d,0} & \mathbf{X} \in \Gamma_{d,0} \end{array} \right., \quad (6)$$

$\bar{\mathbf{u}}_0$ and $\bar{\mathbf{t}}_0$ indicate the prescribed displacement and traction respectively. The strong form has been presented in terms of the nominal stress \mathbb{P} as the work conjugate of the deformation gradient \mathbf{F} to set the scene for the imposition of displacement field through a variational formulation. The strong form can also
 115 be rewritten in terms of the Cauchy (true) stress in the current configuration:

$$\left\{ \begin{array}{ll} \nabla_{\mathbf{x}} \cdot \boldsymbol{\sigma} = 0 & \mathbf{x} \in \Omega \\ \mathbf{u} = \bar{\mathbf{u}} & \mathbf{x} \in \Gamma_u \\ \mathbf{n} \cdot \boldsymbol{\sigma} = \bar{\mathbf{t}} & \mathbf{x} \in \Gamma_t \\ \mathbf{n}_{\Gamma_d} \cdot \boldsymbol{\sigma} = \mathbf{t}_d & \mathbf{x} \in \Gamma_d \end{array} \right., \quad (7)$$

where \mathbf{n} is the vector normal to the external traction surface, see Figure 1.

2.3. Cohesive-zone model at the discontinuity

A mode-I fracture governs this paper. Tractions normal to a discontinuity can be cast as an exponential decay function of the corresponding crack opening.

$$\mathbf{t}_n^{\text{loc}} = f_t \exp\left(-\frac{f_t}{G_f} \kappa\right). \quad (8)$$

120 κ denotes the history parameter, f_t indicate the fracture strength and G_f is the fracture toughness. A Kuhn-Tucker condition governs the loading policy to render the opening irreversible.

$$f(\llbracket u_n \rrbracket, \kappa) = \llbracket u_n \rrbracket - \kappa \leq 0 \quad \dot{\kappa} \geq 0 \quad \dot{\kappa} f = 0 \quad (9)$$

where $\llbracket \mathbf{u}_n \rrbracket$ is the normal displacement jump. Use of the traction-separation relationship in a Newton-Raphson iterative scheme necessitates linearisation of
125 such formulation after a transfer to the global coordinates by:

$$\mathbf{t}_n = \mathbf{Q} \cdot \mathbf{t}_n^{\text{loc}} \quad (10)$$

where \mathbf{Q} is the rotation matrix transforming the local to the global coordinate system. Also, to obtain a symmetric tangent, shear stiffness ought to be neglected. Interested reader is referred to [11] for the linearised formulation.

3. Variational formulation and linearised weak form

130 Herein, the scene is set for the discretisation at the hands of the variational formulation and the linearisation technique.

3.1. Variational formulation

Adopting the principle of virtual work, the weak form of Equation (6) in the reference configuration reads,

$$\int_{\Omega_0} \nabla_{\mathbf{x}} \boldsymbol{\eta} : \mathbb{P} d\Omega - \int_{\Gamma_{t,0}} \boldsymbol{\eta} \cdot \bar{\mathbf{t}} d\Gamma = 0 \quad (11)$$

135 which must hold for all admissible variations, including $\boldsymbol{\eta}$ which is comprised of continuous and discontinuous components, $\hat{\boldsymbol{\eta}}$ and $\tilde{\boldsymbol{\eta}}$ respectively [5, 11]. The test function and its gradient read,

$$\boldsymbol{\eta} = \hat{\boldsymbol{\eta}} + \mathcal{H}_{\Gamma_{d,0}} \tilde{\boldsymbol{\eta}} \quad (12a)$$

$$\nabla_{\mathbf{x}} \boldsymbol{\eta} = \nabla_{\mathbf{x}} \hat{\boldsymbol{\eta}} + \mathcal{H}_{\Gamma_{d,0}} (\nabla_{\mathbf{x}} \tilde{\boldsymbol{\eta}}) + 2\delta_{\Gamma_{d,0}} (\tilde{\boldsymbol{\eta}} \otimes \mathbf{n}_{\Gamma_{d,0}}) \quad (12b)$$

Inserting Equations (12a) and (12b) into Equation (11) and utilising the identity $\int_{\Omega} \delta_{\Gamma_d}(\mathbf{x}) \phi(\mathbf{x}) d\Omega = \int_{\Gamma} \phi(\mathbf{x}) d\Gamma$ leads to separate weak forms for contin-
140 uous and discontinuous equations:

$$\int_{\Omega_0} \nabla_{\mathbf{x}} \hat{\boldsymbol{\eta}} : \mathbb{P} d\Omega_0 = \int_{\Gamma_{t,0}} \hat{\boldsymbol{\eta}} \cdot \bar{\mathbf{t}}_0 d\Gamma_0 \quad (13a)$$

$$\int_{\Omega_0} \mathcal{H}_{\Gamma_{d,0}}(\nabla_{\mathbf{x}} \tilde{\boldsymbol{\eta}}) : \mathbb{P} d\Omega_0 + 2 \int_{\Gamma_{d,0}} \tilde{\boldsymbol{\eta}} \cdot \mathbf{t}_{d,0} d\Gamma_0 = \int_{\Gamma_t} \mathcal{H}_{\Gamma_{d,0}} \tilde{\boldsymbol{\eta}} \cdot \bar{\mathbf{t}}_0 d\Gamma_0. \quad (13b)$$

It is noted that the nominal stress \mathbb{P} is asymmetric, partially defined on the current configuration (load vector in the current configuration applied to the reference surface). To obtain a symmetric stress matrix defined entirely on the material configuration, *second Piola-Kirchhoff* stress is utilised by pulling back
 145 the spatial force of the first Piola-Kirchhoff [12], $\boldsymbol{\Sigma} = \mathbf{F}^{-1}\mathbb{P}$. Substituting such relation in the weak forms in Equation (13) yields,

$$\int_{\Omega_0} \nabla_{\mathbf{x}} \hat{\boldsymbol{\eta}} : (\mathbf{F}\boldsymbol{\Sigma}) d\Omega_0 = \int_{\Gamma_{t,0}} \hat{\boldsymbol{\eta}} \cdot \bar{\mathbf{t}}_0 d\Gamma_0 \quad (14a)$$

$$\int_{\Omega_0} \mathcal{H}_{\Gamma_{d,0}}(\nabla_{\mathbf{x}} \tilde{\boldsymbol{\eta}}) : (\mathbf{F}\boldsymbol{\Sigma}) d\Omega_0 + 2 \int_{\Gamma_{d,0}} \tilde{\boldsymbol{\eta}} \cdot (\mathbf{F}\boldsymbol{\Sigma}\mathbf{n}_{\Gamma_{d,0}}) d\Gamma_0 = \int_{\Gamma_{t,0}} \mathcal{H}_{\Gamma_{d,0}} \tilde{\boldsymbol{\eta}} \cdot \bar{\mathbf{t}}_0 d\Gamma_0. \quad (14b)$$

The relationship between the true stress and the second Piola-Kirchhoff stress reads,

$$\boldsymbol{\sigma} := \frac{1}{\det(\mathbf{F})} \mathbf{F}\boldsymbol{\Sigma}\mathbf{F}^T. \quad (15)$$

Next, incorporating the Nanson's relation and the push forward operation into
 150 Equation (13) [5], we can derive the weak forms for true stresses:

$$\int_{\Omega} \nabla_{\mathbf{x}} \hat{\boldsymbol{\eta}} : \boldsymbol{\sigma} d\Omega = \int_{\Gamma_t} \hat{\boldsymbol{\eta}} \cdot \bar{\mathbf{t}} d\Gamma \quad (16a)$$

$$\int_{\Omega} \mathcal{H}_{\Gamma_d}(\nabla_{\mathbf{x}} \tilde{\boldsymbol{\eta}}) : \boldsymbol{\sigma} d\Omega + 2 \int_{\Gamma_d} \tilde{\boldsymbol{\eta}} \cdot \mathbf{t} d\Gamma = \int_{\Gamma_t} \mathcal{H}_{\Gamma_d} \tilde{\boldsymbol{\eta}} \cdot \bar{\mathbf{t}} d\Gamma. \quad (16b)$$

Equations (14) and (16) set the scene for Total and Updated Lagrangian (TL and UL) approaches to solve a geometrically nonlinear problem, respectively. Adopting either TL or UL leads to a slight dissimilarity in general, while they are identical for hyperelasticity [13, 14]. Even though both formulations are
 155 presented in the manuscript we have adopted a TL formulation for our calculations.

3.2. Linearisation of the constitutive equations

To provide the matrix notation of the governing equations, weak forms should be linearised first. Defined on the reference configuration, the rate of
160 the internal virtual work in the left hand side of Equation (14) reads,

$$\delta\dot{W}_{\text{int}}^{\mathbf{a}} = \int_{\Omega_0} \nabla_{\mathbf{x}} \hat{\boldsymbol{\eta}} : (\dot{\mathbf{F}}\boldsymbol{\Sigma}) d\Omega_0 + \int_{\Omega_0} \nabla_{\mathbf{x}} \hat{\boldsymbol{\eta}} : (\mathbf{F}\dot{\boldsymbol{\Sigma}}) d\Omega_0 \quad (17a)$$

$$\begin{aligned} \delta\dot{W}_{\text{int}}^{\mathbf{b}} &= \int_{\Omega_0} \mathcal{H}_{\Gamma_{\text{d},0}}(\nabla_{\mathbf{x}} \tilde{\boldsymbol{\eta}}) : (\dot{\mathbf{F}}\boldsymbol{\Sigma}) d\Omega_0 + \int_{\Omega_0} \mathcal{H}_{\Gamma_{\text{d},0}}(\nabla_{\mathbf{x}} \tilde{\boldsymbol{\eta}}) : (\mathbf{F}\dot{\boldsymbol{\Sigma}}) d\Omega_0 \\ &+ 2 \int_{\Gamma_{\text{d},0}} \tilde{\boldsymbol{\eta}} \cdot (\dot{\mathbf{F}}\boldsymbol{\Sigma} \mathbf{n}_{\Gamma_{\text{d},0}}) d\Gamma_0 + 2 \int_{\Gamma_{\text{d},0}} \tilde{\boldsymbol{\eta}} \cdot (\mathbf{F}\dot{\boldsymbol{\Sigma}} \mathbf{n}_{\Gamma_{\text{d},0}}) d\Gamma_0 \end{aligned} \quad (17b)$$

while superscripts **a** and **b** denote the standard and enhanced fields corresponding to the continuous and discontinuous fields respectively. The rate of the deformation gradient reads,

$$\dot{\mathbf{F}} = \frac{\partial \mathbf{v}}{\partial \mathbf{X}} = \frac{\partial \mathbf{v}}{\partial \mathbf{x}} \frac{\partial \mathbf{x}}{\partial \mathbf{X}} = \mathbf{lF} \quad (18)$$

where \mathbf{v} is the velocity and \mathbf{l} is the velocity gradient. To present the linearised
165 formulation in the spatial configuration, Equation (17) becomes,

$$\delta\dot{W}_{\text{int}}^{\mathbf{a}} = \int_{\Omega_0} (\nabla_{\mathbf{x}} \hat{\boldsymbol{\eta}}) \mathbf{F} : (\mathbf{lF}\boldsymbol{\Sigma}) d\Omega_0 + \int_{\Omega_0} (\nabla_{\mathbf{x}} \hat{\boldsymbol{\eta}}) \mathbf{F} : (\mathbf{F}\dot{\boldsymbol{\Sigma}}) d\Omega_0 \quad (19a)$$

$$\begin{aligned} \delta\dot{W}_{\text{int}}^{\mathbf{b}} &= \int_{\Omega_0} \mathcal{H}_{\Gamma_{\text{d},0}}(\nabla_{\mathbf{x}} \tilde{\boldsymbol{\eta}}) \mathbf{F} : (\mathbf{lF}\boldsymbol{\Sigma}) d\Omega_0 + \int_{\Omega_0} \mathcal{H}_{\Gamma_{\text{d},0}}(\nabla_{\mathbf{x}} \tilde{\boldsymbol{\eta}}) \mathbf{F} : (\mathbf{F}\dot{\boldsymbol{\Sigma}}) d\Omega_0 \\ &+ 2 \int_{\Gamma_{\text{d},0}} \tilde{\boldsymbol{\eta}} \cdot \left(\mathbf{lF}\boldsymbol{\Sigma} \frac{1}{\det(\mathbf{F})} \mathbf{F}^{\text{T}} \mathbf{n}_{\Gamma_{\text{d}}} \frac{d\Gamma}{d\Gamma_0} \right) d\Gamma_0 \\ &+ 2 \int_{\Gamma_{\text{d},0}} \tilde{\boldsymbol{\eta}} \cdot \left(\mathbf{F}\dot{\boldsymbol{\Sigma}} \frac{1}{\det(\mathbf{F})} \mathbf{F}^{\text{T}} \mathbf{n}_{\Gamma_{\text{d}}} \frac{d\Gamma}{d\Gamma_0} \right) d\Gamma_0 \end{aligned} \quad (19b)$$

leading to,

$$\delta\dot{W}_{\text{int}}^{\mathbf{a}} = \int_{\Omega} \nabla_{\mathbf{x}} \hat{\boldsymbol{\eta}} : (\mathbf{l}\boldsymbol{\sigma}) d\Omega + \int_{\Omega} \nabla_{\mathbf{x}} \hat{\boldsymbol{\eta}} : \dot{\boldsymbol{\sigma}} d\Omega \quad (20a)$$

$$\begin{aligned} \delta \dot{W}_{\text{int}}^{\mathbf{b}} &= \int_{\Omega} \mathcal{H}_{\Gamma_d}(\nabla_{\mathbf{x}} \tilde{\boldsymbol{\eta}}) : (\mathbf{l}\boldsymbol{\sigma}) d\Omega + \int_{\Omega_0} \mathcal{H}_{\Gamma_d} \nabla_{\mathbf{x}} \tilde{\boldsymbol{\eta}} : \overset{\circ}{\boldsymbol{\sigma}} d\Omega \\ &+ 2 \int_{\Gamma_d} \tilde{\boldsymbol{\eta}} \cdot (\mathbf{l}\boldsymbol{\sigma} \mathbf{n}_{\Gamma_d}) d\Gamma + 2 \int_{\Gamma_d} \tilde{\boldsymbol{\eta}} \cdot (\overset{\circ}{\boldsymbol{\sigma}} \mathbf{n}_{\Gamma_d}) d\Gamma \end{aligned} \quad (20b)$$

with $\overset{\circ}{\boldsymbol{\sigma}}$ the Trusdell rate of the Cauchy stress which can be expressed in terms of the rate of deformation tensor $\mathbf{d} = (\mathbf{1} + \mathbf{1}^{\mathbf{T}})/2$,

$$\overset{\circ}{\boldsymbol{\sigma}} = \frac{1}{\det(\mathbf{F})} \mathbf{F} \dot{\boldsymbol{\Sigma}} \mathbf{F}^{\mathbf{T}} \quad (21a)$$

$$\overset{\circ}{\boldsymbol{\sigma}} = \boldsymbol{\mathcal{C}} : \mathbf{d}. \quad (21b)$$

It is also noted that, for the reference configuration, the rate of the second
170 Piola-Kirchhoff stress reads,

$$\dot{\boldsymbol{\Sigma}} = \boldsymbol{\mathcal{C}} : \dot{\mathbf{E}}. \quad (22)$$

while $\boldsymbol{\mathcal{C}}$ and $\boldsymbol{\mathcal{C}}$ being the fourth-order spatial and reference constitutive tensors respectively. $\dot{\mathbf{E}}$ denotes the rate of the Green-Lagrange strain tensor [12].

4. Discrete equations for XIGA

Now, we can cast the linearised formulation in the discrete matrix notation
175 format. First, we need to define Non-Uniform Rational B-Splines (NURBS) as the set of basis function utilised here for IGA. Using such bases, the position field, i.e. Equation (1), can be expressed in terms of NURBS in a discrete format.

4.1. Bézier extraction based NURBS

180 Using the tensor product, a NURBS surface can be cast in terms of the control points \mathbf{p} ,

$$\mathbf{S}(\xi, \eta) = \sum_{k=1}^n \sum_{l=1}^m R_{k,l}^{p,q}(\xi, \eta) \mathbf{p}_{k,l} \quad (23)$$

with the bivariate NURBS basis function [15]:

$$R_{k,l}^{p,q}(\xi, \eta) = \frac{M_{l,q}(\eta)N_{k,p}(\xi)w_{k,l}}{\sum_{\hat{k}}^n \sum_{\hat{l}}^m M_{\hat{k},q}(\eta)N_{\hat{l},p}(\xi)w_{\hat{k},\hat{l}}}. \quad (24)$$

w_k is the weight of the corresponding knot. N and M are B-spline basis functions defined on the Bézier extraction [15, 16] as an element-wise framework to comply with the finite element data structure (see Figure 3):

$$\mathbf{N}^e = \mathbf{C}^e \mathbf{B} \quad (25)$$

185 where superscript e indicates the element index and \mathbf{C} is referred to as Bézier extraction operator. \mathbf{B} denotes the bivariate Bernstein polynomial, see Equation (26), whose input domain is defined on $[-1, 1]$ in Equation (27) to facilitate the integration [15].

$$\mathcal{B}_{k,l}^{p,q}(\xi, \eta) = \mathcal{B}_{k,p}(\xi) \otimes \mathcal{B}_{l,q}(\eta). \quad (26)$$

$$\mathcal{B}_{k,p}(\xi) = \frac{1}{2}(1 - \xi)\mathcal{B}_{k,p-1}(\xi) + \frac{1}{2}(1 + \xi)\mathcal{B}_{k-1,p-1}(\xi) \quad (27a)$$

$$\mathcal{B}_{1,0}(\xi) \equiv 1 \quad (27b)$$

$$\mathcal{B}_{k,p}(\xi) \equiv 0 \quad \text{if } k < 1 \quad \text{or} \quad k > p + 1. \quad (27c)$$

For a comprehensive study on the formulation and derivatives [11] is referred.

190 4.2. Discretised equations

Herein, discrete equations will be cast in terms of NURBS for a Total Lagrangian approach. Updated Lagrangian formulation is presented in the appendix. The position field presented in Equation (1) can be rewritten for NURBS as,

$$\mathbf{x} = \mathbf{X} + \mathbf{R}\mathbf{a} + \mathcal{H}_{\Gamma_{d,0}} \mathbf{R}\mathbf{b}. \quad (28)$$

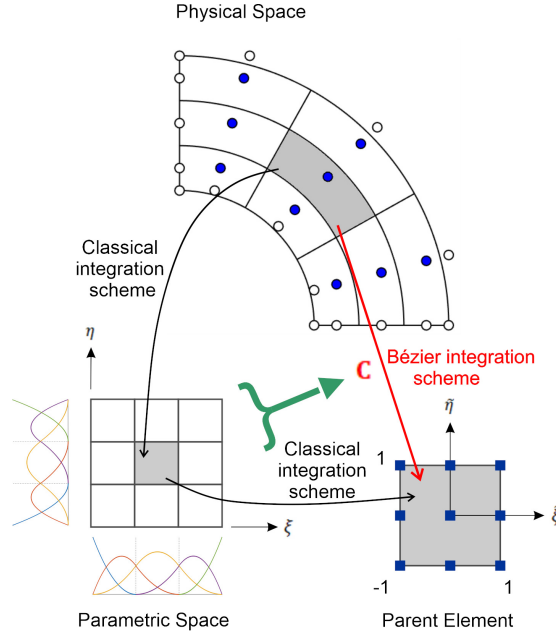


Figure 3: Bézier integration scheme developed on the Bézier extraction operator C . A comparison has been made between classical integration and the Bézier extraction-based integration scheme.

195 Next, we define differential operators which will be utilised for derivation of the strain-displacement relationship and the stiffness matrix,

$$\mathbf{L}_0^T = \mathbf{F} \begin{bmatrix} \frac{\partial}{\partial \mathbf{X}_1} & 0 & \frac{\partial}{\partial \mathbf{X}_2} \\ 0 & \frac{\partial}{\partial \mathbf{X}_2} & \frac{\partial}{\partial \mathbf{X}_1} \end{bmatrix} = \begin{bmatrix} F_{11} \frac{\partial}{\partial x_1} & F_{12} \frac{\partial}{\partial x_2} & F_{11} \frac{\partial}{\partial x_2} + F_{12} \frac{\partial}{\partial x_1} \\ F_{21} \frac{\partial}{\partial x_1} & F_{22} \frac{\partial}{\partial x_2} & F_{21} \frac{\partial}{\partial x_2} + F_{22} \frac{\partial}{\partial x_1} \end{bmatrix}, \quad (29a)$$

$$\bar{\mathbf{L}}_0^T = \begin{bmatrix} \frac{\partial}{\partial \mathbf{X}_1} & \frac{\partial}{\partial \mathbf{X}_2} & 0 & 0 \\ 0 & 0 & \frac{\partial}{\partial \mathbf{X}_1} & \frac{\partial}{\partial \mathbf{X}_2} \end{bmatrix}, \quad (29b)$$

where \mathbf{F} is the deformation gradient. Descriptised matrix notation of the linearised weak forms reads,

$$[\mathbf{K}_{\text{mat}} + \mathbf{K}_{\text{geo}}] \begin{bmatrix} \Delta \mathbf{a} \\ \Delta \mathbf{b} \end{bmatrix} = \begin{bmatrix} \mathbf{f}_a^{\text{ext}} \\ \mathbf{f}_b^{\text{ext}} \end{bmatrix} - \begin{bmatrix} \mathbf{f}_a^{\text{int}} \\ \mathbf{f}_b^{\text{int}} \end{bmatrix}. \quad (30)$$

To express discrete equations in the reference configuration, Equation (17) is considered. Defining \mathbf{B}_N and \mathbf{B}_G ,

$$\mathbf{B}_N = \mathbf{L}_0 \mathbf{N}, \quad (31a)$$

$$\mathbf{B}_G = \bar{\mathbf{L}}_0 \mathbf{N}. \quad (31b)$$

External and internal forces in Equation (30) can be defined in the reference configuration,

$$\mathbf{f}_a^{\text{ext}} = \int_{\Gamma_{t,0}} \mathbf{R}^T \bar{\mathbf{t}}_0 \, d\Gamma_0 \quad (32a)$$

$$\mathbf{f}_b^{\text{ext}} = \int_{\Gamma_{t,0}} \mathcal{H}_{\Gamma_{d,0}} \mathbf{R}^T \bar{\mathbf{t}}_0 \, d\Gamma_0 \quad (32b)$$

$$\mathbf{f}_a^{\text{int}} = \int_{\Omega_0} \mathbf{B}_N^T \boldsymbol{\Sigma} \, d\Omega \quad (32c)$$

$$\mathbf{f}_b^{\text{int}} = \int_{\Omega_0} \mathcal{H}_{\Gamma_{d,0}} \mathbf{B}_N^T \boldsymbol{\Sigma} \, d\Omega_0 + 2 \int_{\Gamma_{d,0}} \mathbf{R}^T \mathbf{t}_{d,0} \, d\Gamma_0 \quad (32d)$$

and the material and geometric parts of the stiffness matrices become:

$$\mathbf{K}_{\text{mat}} := \begin{bmatrix} \mathbf{K}_{\text{mat}}^{\text{aa}} & \mathbf{K}_{\text{mat}}^{\text{ab}} \\ \mathbf{K}_{\text{mat}}^{\text{ba}} & \mathbf{K}_{\text{mat}}^{\text{bb}} \end{bmatrix} \quad (33a)$$

$$\mathbf{K}_{\text{mat}}^{\text{aa}} = \int_{\Omega_0} \mathbf{B}_N^T : \mathcal{C} : \mathbf{B}_N \, d\Omega_0 \quad (33b)$$

$$\mathbf{K}_{\text{mat}}^{\text{ab}} = \int_{\Omega_0} \mathcal{H}_{\Gamma_{d,0}} \mathbf{B}_N^T : \mathcal{C} : \mathbf{B}_N \, d\Omega_0 \quad (33c)$$

$$\mathbf{K}_{\text{mat}}^{\text{ba}} = \int_{\Omega_0} \mathcal{H}_{\Gamma_{d,0}} \mathbf{B}_N^T : \mathcal{C} : \mathbf{B}_N \, d\Omega_0 \quad (33d)$$

$$\mathbf{K}_{\text{mat}}^{\text{bb}} = \int_{\Omega_0} \mathbf{B}_N^T : \mathcal{C} : \mathbf{B}_N \, d\Omega_0 + 4 \int_{\Gamma_{d,0}} \mathbf{R}^T \mathbf{Q}^T : \mathbf{T}_d : \mathbf{Q} \mathbf{R} \, d\Gamma_0 \quad (33e)$$

$$\mathbf{K}_{\text{geo}} := \begin{bmatrix} \mathbf{K}_{\text{geo}}^{\text{aa}} & \mathbf{K}_{\text{geo}}^{\text{ab}} \\ \mathbf{K}_{\text{geo}}^{\text{ba}} & \mathbf{K}_{\text{geo}}^{\text{bb}} \end{bmatrix} \quad (34a)$$

$$\mathbf{K}_{\text{geo}}^{\text{aa}} = \int_{\Omega_0} \mathbf{B}_G^T \bar{\boldsymbol{\Sigma}} \mathbf{B}_G \, d\Omega_0 \quad (34b)$$

$$\mathbf{K}_{\text{geo}}^{\text{ab}} = \int_{\Omega_0} \mathcal{H}_{\Gamma_{d,0}} \mathbf{B}_G^T \bar{\boldsymbol{\Sigma}} \mathbf{B}_G \, d\Omega_0 \quad (34c)$$

$$\mathbf{K}_{\text{geo}}^{\text{ba}} = \int_{\Omega_0} \mathcal{H}_{\Gamma_{d,0}} \mathbf{B}_G^T \bar{\boldsymbol{\Sigma}} \mathbf{B}_G \, d\Omega_0 + 2 \int_{\Gamma_{d,0}} \bar{\mathbf{R}}^T \bar{\mathbf{t}}_{d,0} \mathbf{B}_G \, d\Gamma_0 \quad (34d)$$

$$\mathbf{K}_{\text{geo}}^{\text{bb}} = \int_{\Omega_0} \mathbf{B}_G^T \bar{\boldsymbol{\Sigma}} \mathbf{B}_G \, d\Omega_0 + 2 \int_{\Gamma_{d,0}} \mathcal{H}_{\Gamma_{d,0}} \bar{\mathbf{R}}^T \bar{\mathbf{t}}_{d,0} \mathbf{B}_G \, d\Gamma_0 \quad (34e)$$

with \mathbf{Q} denoting the rotation matrix. Also,

$$\bar{\boldsymbol{\Sigma}} := \begin{bmatrix} \Sigma_{11} & \Sigma_{12} & 0 & 0 \\ \Sigma_{21} & \Sigma_{22} & 0 & 0 \\ 0 & 0 & \Sigma_{11} & \Sigma_{12} \\ 0 & 0 & \Sigma_{21} & \Sigma_{22} \end{bmatrix} \quad (35a)$$

$$\bar{\mathbf{R}} := \begin{bmatrix} \mathbf{R}_1 & \cdots & \mathbf{R}_m & 0 & \cdots & 0 \\ 0 & \cdots & 0 & \mathbf{R}_1 & \cdots & \mathbf{R}_m \end{bmatrix}. \quad (35b)$$

$$\bar{\mathbf{t}}_{d,0} := \begin{bmatrix} \bar{t}_{d,0,1} & \bar{t}_{d,0,2} & 0 & 0 \\ 0 & 0 & \bar{t}_{d,0,1} & \bar{t}_{d,0,2} \end{bmatrix}. \quad (35c)$$

205 where m is the number of enriched control points within the element under consideration.

5. Implementation aspects

To cast the aforementioned formulation in a finite element datastructure some numerical aspects have to be considered. Specially, dealing with IGA, the shared inter-element control points complicate the enrichment and the compat-
210 ability imposition between multiple displacement fields which are adopted for

XIGA. Though this has been comprehensively studied in [11], key points are briefly re-stated here to fulfill the uniformity of the current manuscript.

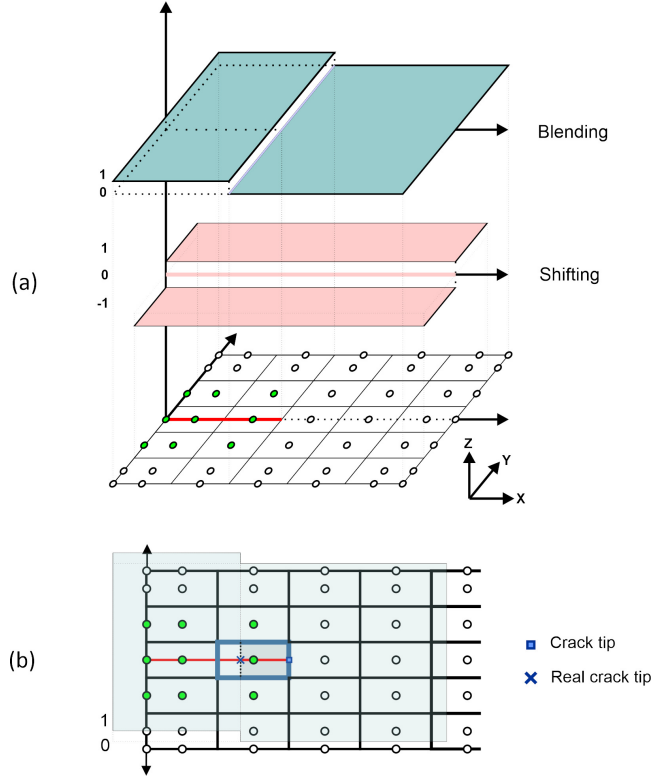


Figure 4: Compatibility enforcement for a quadratic interpolation under mode-I fracture: (a) Shifting technique is defined on the sign function in Equation (2), while a step function is adopted for the blending technique where the element is fully cracked. The blending technique is illustrated for a partially cracked element in (b). *Crack tip* governs the enrichment scheme while *real crack tip* shows the last location where fracture criterion is satisfied [11].

5.1. Compatibility enforcement

215 *Shifting* and *blending* techniques [11] are utilised to enforce compatibility. Unlike extended finite element analysis whose Lagrange interpolation localises the shifted Heaviside function inside the cracked elements, shifting narrows this effect to the adjacent elements perpendicular to the crack path for B-splines, see Figure 4. This stems from the C^0 -continuity used in FEM and a higher

220 interpolation-order in IGA at element boundaries. The latter leads to a stretch
of the discontinuity effect over multiple rows of elements compared to the single
row of cracked elements in XFEM. Shifting should be applied to discontinuous
terms, i.e. all the Heaviside terms in discretised equations have to be shifted.
Owing to the same reason, the effect of Heaviside function which redundantly
225 appears in front of the crack tip ought to be removed. Therefore, a step function
has been utilised as the blending technique, which has been elaborated on in
[11]. Shifted basis functions are illustrated for a univariate and bivariate NURBS
bases in Figure 5, where it is realised of intact and cracked media.

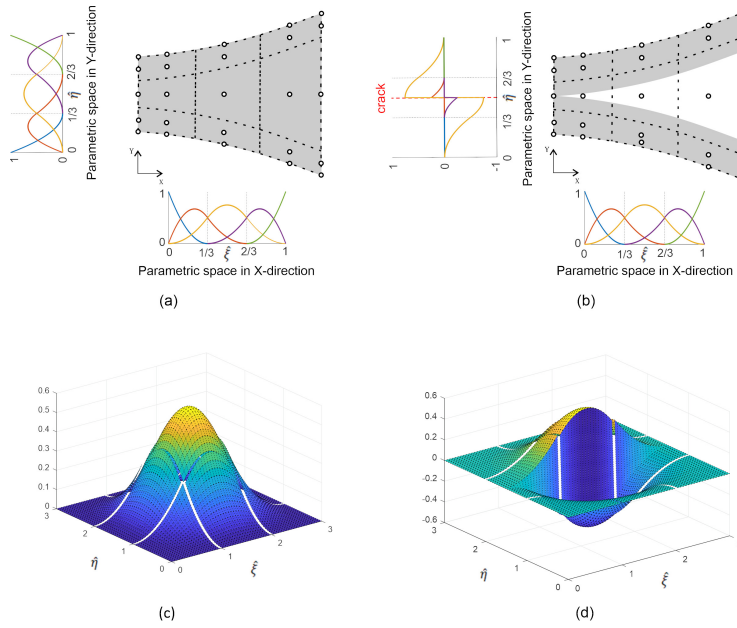


Figure 5: Shifted basis functions for a quadratic interpolation under mode-I fracture: univariate NURBS basis functions are shown for intact (a) and shifted discontinuous medium (b). Adopting the tensor product concept to elevate the dimension, bivariate surfaces of intact (c) and shifted discontinuous medium (d) are illustrated for the control point in the middle of the medium, i.e. tensor product of the yellow curves in (a) and (b).

230 *Remark 1.* A plate with 7 equally distanced elements has been illustrated in
Figure 6. The crack is located in the middle of the plate, inside the 4th element,
whose enhanced control points are illustrated in red asterisks. Updated

Lagrangian formulation necessitates the position field, Equation (28), to be updated in each iteration. As mentioned previously, compatibility enforcement aims to localise the effect of the Heaviside function to the cracked element, but
 235 fails to do so within the use of B-splines owing to the inter-element share of control points. Figure 6 illustrates the shifted Heaviside function values for the enhanced points (red asterisks), which are supposed to be zero. For the asterisks above and below crack path, however, these values render the undesired enhanced field to become non-zero at the location of the control points, see the
 240 last term in Equation (28). Our observations suggest exempting this undesired term during the position field update. Otherwise, it slows down the convergence rate and/or subsequently diverges the solution. This suggests that the compatibility between the two fields has not fully enforced (otherwise, enhanced term would become zero at the location of control points), though it has significantly
 245 improved previous attempts within XIGA contributions [11].

Remark 2. Based on *remark 1* and the need to update the crack profile for cohesive traction integration in UL, TL seems to be a more convenient choice within XIGA from an implementation perspective since it merely affects the stiffness matrix and internal force. Therefore, no extra action, such as any
 250 update, is required in each iteration.

Remark 3. Although the Heaviside value at crack path $\Gamma_{d,0}$ equals zero, the last term presented in Equation (34e) will remain owing to the compatibility enforcement. It is important to recall that the discretised formulation concluded from the variational formulation are not shifted, and shifting affects only after
 255 discretisation [11]. Accordingly, the Heaviside integrand in Equation (34e) becomes $\mathcal{H}_{\Gamma_{d,0}} - \mathcal{H}_0^{\mathbb{B}}$, where $\mathcal{H}_0^{\mathbb{B}}$ denote the Heveaside value for control points in the reference configuration. Therefore, based on the Heaviside sign function, $\mathcal{H}_{\Gamma_{d,0}}$ becomes zero but $\mathcal{H}_0^{\mathbb{B}}$ will contain a value (-1, 0 or 1) which preserves this term in Equation (34e). This is exempted in [5].

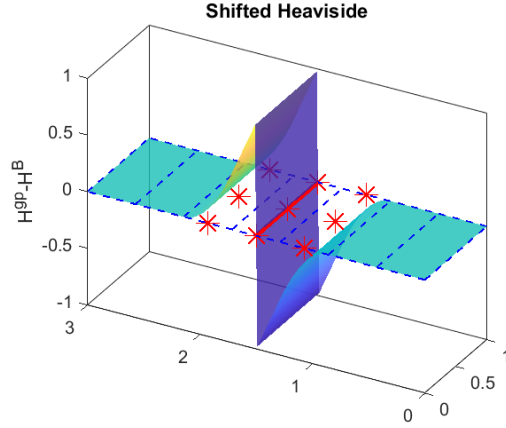


Figure 6: Domain excess of the shifted Heaviside from the cracked element. Red asterisks denote the enhanced control points, where shifted Heaviside value differs from zero. H^{GP} and H^{B} denote Heaviside values for Gauss points and control points respectively.

260 *5.2. Other implementation aspects*

Herein, we tend to succinctly enumerate necessary implementation aspects. The interested reader is referred to [11] for a detailed discussion.

Crack extension. Several factors must be considered when propagating a crack, e.g. crack extension direction, propagation criterion and the geometry of the extension. Similar to XFEM [5, 17] and XIGA [11], a non-local approach is adopted here to mitigate inaccurate local estimation of stresses, though improved by IGA yet insufficient when cracks are confronted [11]. Once crack path is found, stresses along the path are being compared to the fracture strength. In this manuscript, propagation occurs when half of the Gauss points along the crack path satisfy $\sigma_y^{\text{loc}} \geq f_t$. Next, crack propagates as a straight line throughout the element and the *crack tip* will be defined at the intersection of crack path and the edge of the element, see Figure 4b. It is noted that some sections of the new crack path might not have met the fracture criterion yet. Adopting a blending technique, these sections will be neglected from the integration process [11]. Hence, the *real crack tip* can be defined on the location where fracture criterion has been lastly satisfied, see Figure 4b.

270
275

Individual control points enhancement. As mentioned previously, crack crosses the element entirely in the form of a straight line, and finishes at the edge of the element to pinpoint the crack tip. Enrichment of the element follows the crack tip, and not the real crack tip: points at or in front of the crack tip will be precluded since the crack tip is closed in cohesive fracture. It is important to invoke that inter-element sharing of the control points in XIGA causes such complication, while the C^0 -continuity which underlies the Lagrangian interpolation in XFEM changes this enrichment prescription into a mere exemption of the points at the location of the crack tip.

Integration scheme and point projection. Gauss integration scheme is adopted for any integration operation in this manuscript. Sub-triangulation technique is utilised for elements crossed by the crack path to guarantee adequate number of Gauss points at each side of the crack. To impose the cohesive tractions on the crack path, line integration is required. Exploiting interface elements [4, 18, 19, 20], degrees of freedom are defined explicitly for the crack path, i.e. there exists a physical definition of the discontinuity. In an extended approach, however, discontinuity is embedded inside the element in an arbitrary mesh lay-out, where degrees of freedom belong to the element and not to the discontinuity. Hence, in order to integrate the line on the element's degrees of freedom, natural coordinates on the parent line should be mapped onto the parent square while the location of crack inside the element being considered. This requires point projection scheme, which is comprehensively studied in [11] with adequate mathematical background.

6. Numerical examples

In this section some numerical examples are presented to validate the aforementioned method and implementation aspects. These examples each aim to verify a specific objective, one at a time. Results are compared with XFEM [5].

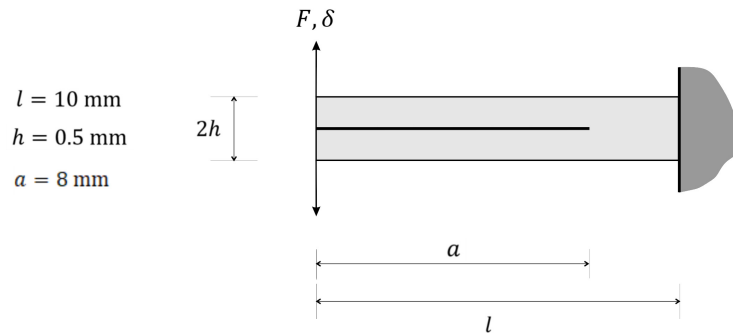


Figure 7: Double Cantilever Beam with a traction-free initial slit. Propagation is prevented. F and δ are the force and displacement here, and in the remainder of manuscript.

6.1. Explicit and enhanced discontinuity modelling: Double Cantilever Beam

305 The first example assesses the geometric nonlinearity in the presence of a discontinuity. It is fulfilled in two ways, by means of a non-progressive explicit interface and a peel test. A Double Cantilever Beam (DCB) is exploited for both cases.

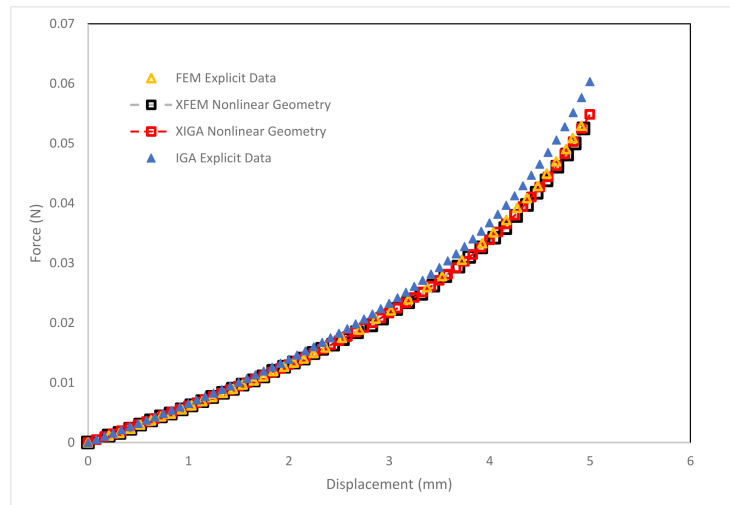


Figure 8: Results of the explicitly modelled fixed interface for a DCB.

6.1.1. Explicit interface

310 A traction-free slit is modelled within a DCB problem, see Figure 7, while any further propagation is prevented. Young’s modulus and Poisson’s ratio are taken $E = 100$ MPa and $\nu = 0.3$ respectively. The analysis comprises two approaches, interface elements and the extended scheme, while results are compared to the finite element analysis counterparts.

315 Results show an excellent agreement between XIGA and XFEM, while there exists a negligible difference between IGA and FEM interface elements at the last few loading steps. The reason lies in the use of dummy stiffness (or penalty parameter) to keep the the delamination closed after the slit. Owing to the reason that control points are shared between elements in IGA, use of dummy stiffness renders the last delaminated interface element semi-open (because of
 320 the last control point of this element being shared with the first intact element after delamination). This results in a stiffer response from IGA interface element approach when the opening reaches the end of the delamination, which happens at the last few loading steps. By the way of contrast, dummy stiffness is not needed in an extended approach, and this is the reason no dissimilarity
 325 is observed between XFEM and XIGA.

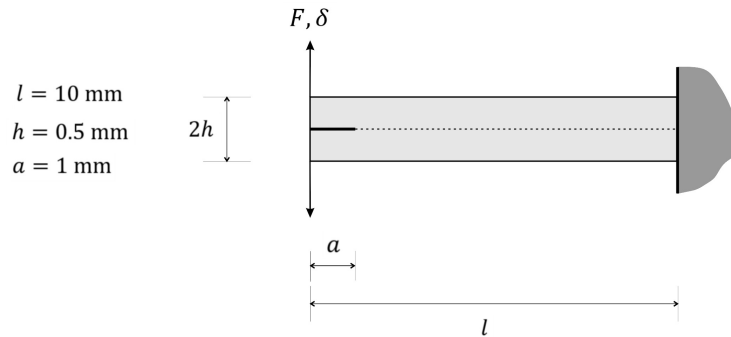


Figure 9: Crack propagation for a DCB under mode-I loading.

6.1.2. Peel test

Now the assumption of propagation prevention is released. The initial slit is shortened to 1mm, see the geometry in Figure 9. Same material properties from the previous section are used here, while the tensile stress and fracture energy read $f_t = 1$ MPa and $G_f = 0.05$ N · mm⁻¹ respectively. It is noted that only the extended approach is employed here.

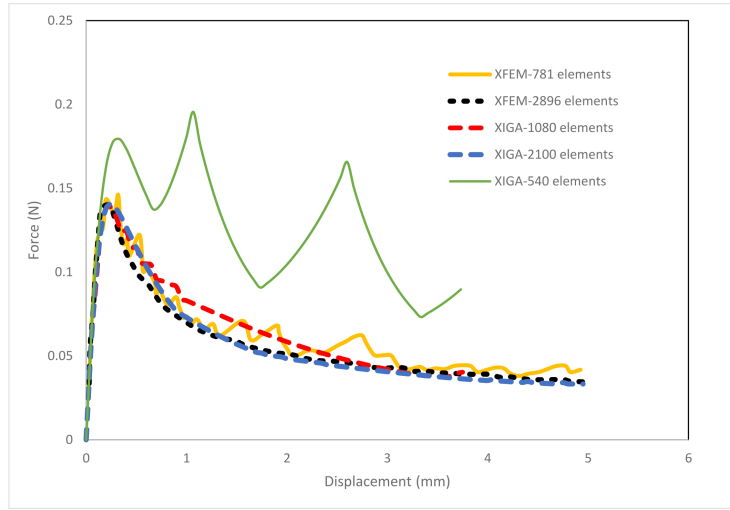


Figure 10: Results of the peel test for a DCB.

Results are presented in Figure 10. We can see a convergence trend for XIGA, concluded with the finest mesh (blue dashed line with 2100 elements) which is much less than finest mesh utilised in XFEM (black dashed line with 2896 elements). Also for the red dashed line (XIGA 1080 elements) is smoother than the yellow one (XFEM 781 elements). Though they share the same peak, responses are slightly different. The coarsest mesh (540 elements shown with the green line) for XIGA illustrates a disparity compared to other data due to the super coarse mesh used, i.e. the same mesh utilised in small displacement [11] is adopted here whose cohesive interface propagation is much bigger than the small deformation case. Therefore, this discretisation is incapable of yielding the correct result, and the effect of the mesh refinement on achieving the correct

solution [21], especially for a cohesive crack propagation test [11], is apparent.

345 As also mentioned in [5], interface linearisation requires severe rotations and consequently dissimilar normal vectors for the profile and sides of the crack, as observed in Figure 1. This becomes more interesting when sign function is adopted here compared to the step function used in [5], rendering a difference on explicit definition of the normal vector for the crack path and the integration
 350 of Gauss points located on this path. Therefore, new examples have to be examined for a full assessment of the linearised formulation.

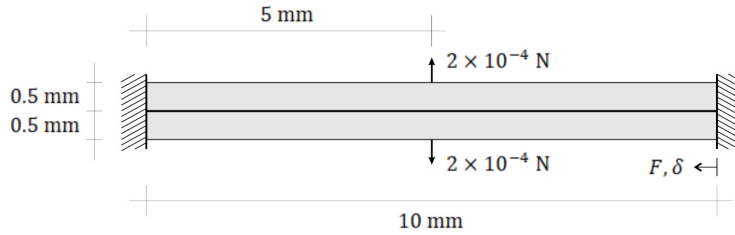


Figure 11: Compression applied to a DCB to rener the buckling failure mode.

6.2. Geometric instability: buckling in composites

To challenge the capability of the proposed formulation to handle geometric instabilities, a buckling test is examined. A DCB, the geometry is given in
 355 Figure 11, is subjected to compression and a negligible perturbation (small lateral loads) to trigger the buckling. This phenomenon happens frequently in laminated composites, where layers are slender and prone to this failure mode. Instead of modelling a peel test, it is assumed that the delamination has already happened throughout the beam (illustrated with the solid black line).
 360 Therefore, no cohesive traction exists on the interface. Similar to previous examples, Young's modulus is taken as $E = 100 \text{ MPa}$, while two values are adopted for Poisson's ratio, $\nu = 0$ and $\nu = 0.3$.

An excellent agreement is observed between XIGA and XFEM results for both values of poisson's ratio, see Figure 12. Another noteworthy aspect is the
 365 fewer number of elements used in XIGA (355 elements) compared to XFEM (781

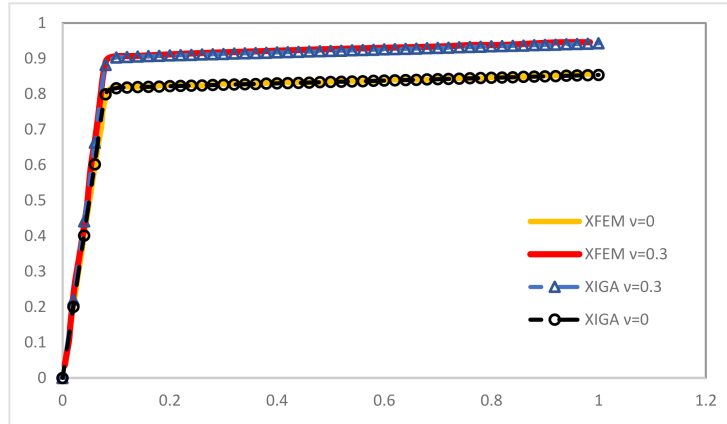


Figure 12: Results of the XIGA buckling test compared with XFEM.

elements), which is legitimate given the fact that the inter-element higher-order continuity allows for a decrease in the number of elements (and consequently a decrease in degrees of freedom) in XIGA. The critical load for a single beam (current results indicate two beams) for $\nu = 0$ matches the Euler buckling load:

$$P_{\text{crit}} = \frac{4\pi^2 EI}{L^2} \approx 0.4112 \quad (36)$$

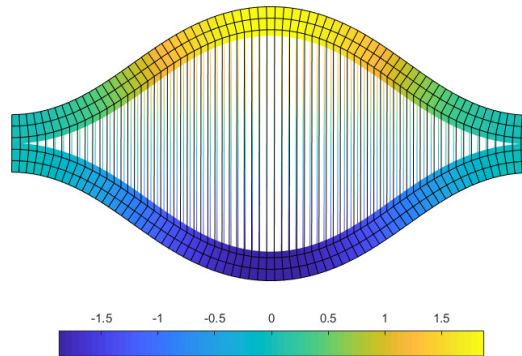


Figure 13: Deformed shape of the buckling test. Colours indicate the deformation in the Y-direction, and numbers in the colour bar are given in millimeters.

370 which has been mentioned in [5] as well. Unmagnified deformed configuration of the buckling test is illustrated in Figure 13.

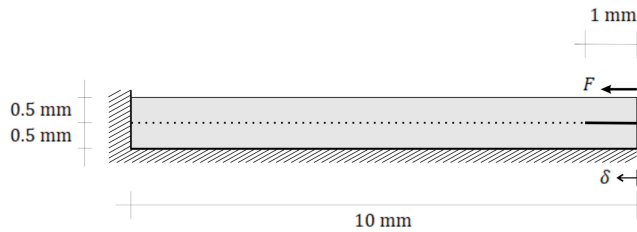


Figure 14: A DCB subjected to a peel test from a stiff substrate.

6.3. Effect of the linearised interface tangent: Peel test from a stiff substrate

Finally, our last example is dedicated to the linearised terms of the interface tangent. For this purpose, one of the layers of the DCB is peeled from the other
 375 one, providing a severe rotation which is ideal for our objective. An initial slit of 1 mm exists in the medium, see Figure 14 for the geometry, followed by a path (dotted line) for a peel test. Unlike the cohesive-zone model section where an exponential decay was recommended, here a constant value equal to the fracture strength is assumed in order to fully maintain the geometric contribution of
 380 cohesive tractions and their linearised tangent terms. Therefore, at the onset of the peeling the normal tractions equal f_t and the material contribution of the interface tangent \mathbf{T} on the stiffness matrix becomes zero [5]. Material properties read: Young's modulus $E = 100\text{MPa}$, Poisson's ratio $\nu = 0.3$ and fracture strength $f_t = 2\text{MPa}$.

Table 1: Energy residuals including/excluding the Linearised Interface Tangent (LIT).

i	XIGA with LIT	XIGA without LIT	XFEM with LIT	XFEM without LIT
0	7.64×10^{-2}	8.40×10^{-2}	3.13×10^0	3.04×10^0
1	6.08×10^{-5}	4.30×10^{-4}	5.62×10^{-2}	3.58×10^{-2}
2	1.13×10^{-6}	2.53×10^{-7}	4.13×10^{-5}	4.72×10^{-4}
3	3.72×10^{-10}	2.05×10^{-13}	4.38×10^{-8}	3.00×10^{-6}
4			5.56×10^{-11}	1.06×10^{-8}
5				4.35×10^{-11}

385 The deformed shape is illustrated in Figure 15. The convergence of the last

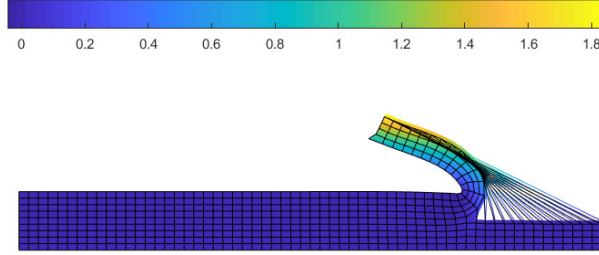


Figure 15: Unmagnified deformed shape of a peel test from a stiff substrate at $u = 4$ mm. Values of the colour bar are given in millimeters, and colours denote the displacement in the Y-direction.

loading step (20th step) is presented in Table 1. Energy residuals illustrated in the table are similar to the ones defined in [5] for the sake of a comparison between XIGA and XFEM:

$$E^i := (\mathbf{du}^i)^T \mathbf{f}_{\text{res}}^i \quad (37)$$

where \mathbf{du}^i is the incremental displacement vector at iteration i and $\mathbf{f}_{\text{res}}^i$ is the residual of force vector at the same iteration [5]. The tolerance for the residual to converge is set $E^i/E^0 < 1 \times 10^{-9}$. From Table 1, it is evident that XIGA converges faster than XFEM. Though the number of elements used for XFEM in [5] has not been reported, fewer elements seems to be used in XIGA (540 elements) by a comparison with the deformed configuration figure presented there. Accounting linearisation of interface tangent or not is the source of contradiction between XFEM and XIGA, since the interface linearised term accelerates the convergence in XFEM. In XIGA, however, though it follows the same trend at the onset of the solution (the first two iterations), linearisation of interface tangent slows down afterwards, i.e. the absence of linearisation speeds up at the third and fourth iterations of XIGA. The reason might be the errors of the compatibility enforcement in linearised interface tangent terms (mentioned in remarks 1 and 3) which aggravate the convergence after a certain iteration onward, see the Heaviside term in Equations 34d and e. Nevertheless, both

cases in XIGA converge at the same number of iterations and excel XFEM.

405 7. Conclusion

In this manuscript, XIGA has been realised of geometric nonlinearity for cohesive fracture. The application targeted has been the delamination for laminated composites. A variety of examples has been examined to challenge every aspect of the geometrically nonlinear formulation. A sign function has been substituted for the step functions utilised in the literature, leading to an explicit definition of the crack path to avoid additional manipulation to define the normal vector for the crack path. Variational formulation has been developed accordingly to achieve discretised formulation. Next, Compatibility enforcement and implementation aspects have been described in details, including extra cares taken exclusively for the case of geometric nonlinearity. It has been shown that XIGA Excels XFEM in terms of the fewer degrees of freedom required and the convergence rate, rendering it an ideal choice to model the delamination in laminated composite undergone geometric nonlinearity.

Acknowledgment

420 Financial support from the European Research Council (Advanced Grant 664734 "PoroFrac") is gratefully acknowledged.

Appendix

Updated Lagrangian description

Similar to the Total Lagrangian approach, we can define the matrix notation governing the Updated Lagrangian formulation,

$$\mathbf{L}_t^{\mathbf{T}} = \begin{bmatrix} \frac{\partial}{\partial \mathbf{x}_1} & 0 & \frac{\partial}{\partial \mathbf{x}_2} \\ 0 & \frac{\partial}{\partial \mathbf{x}_2} & \frac{\partial}{\partial \mathbf{x}_1} \end{bmatrix},$$
$$\bar{\mathbf{L}}_t^{\mathbf{T}} = \begin{bmatrix} \frac{\partial}{\partial \mathbf{x}_1} & \frac{\partial}{\partial \mathbf{x}_2} & 0 & 0 \\ 0 & 0 & \frac{\partial}{\partial \mathbf{x}_1} & \frac{\partial}{\partial \mathbf{x}_2} \end{bmatrix}.$$

$$\mathbf{B}_N = \mathbf{L}_t \mathbf{N},$$

$$\mathbf{B}_G = \bar{\mathbf{L}}_t \mathbf{N}.$$

Recalling Equation (30) we can define the matrices for Updated Lagrangian description,

$$\mathbf{f}_a^{\text{ext}} = \int_{\Gamma_t} \mathbf{R}^T \bar{\mathbf{t}} \, d\Gamma$$

$$\mathbf{f}_b^{\text{ext}} = \int_{\Gamma_t} \mathcal{H}_{\Gamma_d} \mathbf{R}^T \bar{\mathbf{t}} \, d\Gamma$$

$$\mathbf{f}_a^{\text{int}} = \int_{\Omega} \mathbf{B}_N^T \boldsymbol{\sigma} \, d\Omega$$

$$\mathbf{f}_b^{\text{int}} = \int_{\Omega} \mathcal{H}_{\Gamma_d} \mathbf{B}_N^T \boldsymbol{\sigma} \, d\Omega + 2 \int_{\Gamma_d} \mathbf{R}^T \mathbf{t}_d \, d\Gamma$$

$$\mathbf{K}_{\text{mat}} := \begin{bmatrix} \mathbf{K}_{\text{mat}}^{\text{aa}} & \mathbf{K}_{\text{mat}}^{\text{ab}} \\ \mathbf{K}_{\text{mat}}^{\text{ba}} & \mathbf{K}_{\text{mat}}^{\text{bb}} \end{bmatrix}$$

$$\mathbf{K}_{\text{mat}}^{\text{aa}} = \int_{\Omega_0} \mathbf{B}_N^T : \boldsymbol{\epsilon} : \mathbf{B}_N \, d\Omega$$

$$\mathbf{K}_{\text{mat}}^{\text{ab}} = \int_{\Omega} \mathcal{H}_{\Gamma_d} \mathbf{B}_N^T : \boldsymbol{\epsilon} : \mathbf{B}_N \, d\Omega$$

$$\mathbf{K}_{\text{mat}}^{\text{ba}} = \int_{\Omega} \mathcal{H}_{\Gamma_{d,0}} \mathbf{B}_N^T : \boldsymbol{\epsilon} : \mathbf{B}_N \, d\Omega$$

$$\mathbf{K}_{\text{mat}}^{\text{bb}} = \int_{\Omega} \mathbf{B}_N^T : \boldsymbol{\epsilon} : \mathbf{B}_N \, d\Omega + 4 \int_{\Gamma_d} \mathbf{R}^T \mathbf{Q}^T : \mathbf{T}_d : \mathbf{Q} \mathbf{R} \, d\Gamma$$

$$\mathbf{K}_{\text{geo}} := \begin{bmatrix} \mathbf{K}_{\text{geo}}^{\text{aa}} & \mathbf{K}_{\text{geo}}^{\text{ab}} \\ \mathbf{K}_{\text{geo}}^{\text{ba}} & \mathbf{K}_{\text{geo}}^{\text{bb}} \end{bmatrix}$$

$$\mathbf{K}_{\text{geo}}^{\text{aa}} = \int_{\Omega} \mathbf{B}_G^T \bar{\boldsymbol{\sigma}} \mathbf{B}_G \, d\Omega$$

$$\mathbf{K}_{\text{geo}}^{\text{ab}} = \int_{\Omega} \mathcal{H}_{\Gamma_d} \mathbf{B}_G^T \bar{\boldsymbol{\sigma}} \mathbf{B}_G \, d\Omega$$

$$\mathbf{K}_{\text{geo}}^{\text{ba}} = \int_{\Omega} \mathcal{H}_{\Gamma_d} \mathbf{B}_G^T \bar{\boldsymbol{\sigma}} \mathbf{B}_G \, d\Omega + 2 \int_{\Gamma_d} \mathbf{R}^T \bar{\mathbf{t}}_d \mathbf{B}_G \, d\Gamma$$

$$\mathbf{K}_{\text{geo}}^{\text{bb}} = \int_{\Omega} \mathbf{B}_G^T \bar{\boldsymbol{\sigma}} \mathbf{B}_G \, d\Omega + 2 \int_{\Gamma_d} \mathcal{H}_{\Gamma_d} \mathbf{R}^T \bar{\mathbf{t}}_d \mathbf{B}_G \, d\Gamma$$

where,

$$\bar{\boldsymbol{\sigma}} := \begin{bmatrix} \sigma_{11} & \sigma_{12} & 0 & 0 \\ \sigma_{21} & \sigma_{22} & 0 & 0 \\ 0 & 0 & \sigma_{11} & \sigma_{12} \\ 0 & 0 & \sigma_{21} & \sigma_{22} \end{bmatrix}$$

$$\bar{\mathbf{t}}_d := \begin{bmatrix} \bar{t}_{d1} & \bar{t}_{d2} & 0 & 0 \\ 0 & 0 & \bar{t}_{d1} & \bar{t}_{d2} \end{bmatrix}.$$

σ is the Cauchy stress. It is noted that , for Updated Lagrangian, location of
 430 control points and the crack profile needs to be updated in every iterations.

References

- [1] F. Irzal, J. J. Remmers, J. M. Huyghe, R. de Borst, A large deformation
 formulation for fluid flow in a progressively fracturing porous material,
 Computer Methods in Applied Mechanics and Engineering 256 (2013) 29–
 435 37.
- [2] P. Broumand, A. Khoei, The extended finite element method for large
 deformation ductile fracture problems with a non-local damage-plasticity
 model, Engineering Fracture Mechanics 112 (2013) 97–125.
- [3] F. Fathi, S. H. Ardakani, P. F. Dehaghani, S. Mohammadi, A finite strain
 440 integral-type anisotropic damage model for fiber-reinforced materials: Ap-
 plication in soft biological tissues, Computer Methods in Applied Mechanics
 and Engineering 322 (2017) 262–295.
- [4] G. Alfano, M. Crisfield, Finite element interface models for the delami-
 nation analysis of laminated composites: mechanical and computational
 445 issues, International journal for numerical methods in engineering 50 (7)
 (2001) 1701–1736.

- [5] G. Wells, R. De Borst, L. Sluys, A consistent geometrically non-linear approach for delamination, *International Journal for Numerical Methods in Engineering* 54 (9) (2002) 1333–1355.
- 450 [6] I. Babuška, J. M. Melenk, The partition of unity method, *International journal for numerical methods in engineering* 40 (4) (1997) 727–758.
- [7] N. Moës, J. Dolbow, T. Belytschko, A finite element method for crack growth without remeshing, *International journal for numerical methods in engineering* 46 (1) (1999) 131–150.
- 455 [8] T. Belytschko, T. Black, Elastic crack growth in finite elements with minimal remeshing, *International journal for numerical methods in engineering* 45 (5) (1999) 601–620.
- [9] T. Belytschko, N. Moës, S. Usui, C. Parimi, Arbitrary discontinuities in finite elements, *International Journal for Numerical Methods in Engineering* 460 50 (4) (2001) 993–1013.
- [10] E. De Luycker, D. J. Benson, T. Belytschko, Y. Bazilevs, M. C. Hsu, X-fem in isogeometric analysis for linear fracture mechanics, *International Journal for Numerical Methods in Engineering* 87 (6) (2011) 541–565.
- [11] F. Fathi, L. Chen, R. de Borst, Extended isogeometric analysis for cohesive fracture, *International Journal for Numerical Methods in Engineering*.
465 URL <https://doi.org/10.1002/nme.6453>
- [12] J. Bonet, R. D. Wood, *Nonlinear continuum mechanics for finite element analysis*, Cambridge university press, 1997.
- [13] R. de Borst, M. A. Crisfield, J. J. C. Remmers, C. V. Verhoosel, *Nonlinear Finite Element Analysis of Solids and Structures*, John Wiley & Sons, 470 Chichester, 2012.
- [14] K.-J. Bathe, E. Ramm, E. L. Wilson, Finite element formulations for large deformation dynamic analysis, *International journal for numerical methods in engineering* 9 (2) (1975) 353–386.

- 475 [15] M. J. Borden, M. A. Scott, J. A. Evans, T. J. R. Hughes, Isogeometric
finite element data structures based on Bézier extraction of NURBS, *International Journal for Numerical Methods in Engineering* 87 (2011) 15–47.
- [16] R. de Borst, L. Chen, The role of Bézier extraction in adaptive isogeometric
analysis: Local refinement and hierarchical refinement, *International*
480 *Journal for Numerical Methods in Engineering* 113 (2018) 999–1019.
- [17] G. N. Wells, L. Sluys, A new method for modelling cohesive cracks using finite
elements, *International Journal for Numerical Methods in Engineering*
50 (12) (2001) 2667–2682.
- [18] J. Schellekens, R. De Borst, On the numerical integration of interface elements,
485 *International Journal for Numerical Methods in Engineering* 36 (1)
(1993) 43–66.
- [19] J. Vignollet, S. May, R. de Borst, On the numerical integration of isogeometric
interface elements, *International Journal for Numerical Methods in Engineering* 102 (11) (2015) 1733–1749.
- 490 [20] L. Chen, E. J. Lingen, R. de Borst, Adaptive hierarchical refinement of
nurbs in cohesive fracture analysis, *International Journal for Numerical Methods in Engineering* 112 (13) (2017) 2151–2173.
- [21] T. J. Hughes, *The finite element method: linear static and dynamic finite element analysis*, Courier Corporation, 2012.